VNU Journal of Science: Mathematics - Physics

Journal homepage: https://js.vnu.edu.vn/MaP

Original Article

# Numerical Modeling of Turbulent Flows Influencing the Dispersion of Atmospheric Pollutants Around a High-rise Building in an Urban Environment

Faria Quentin[1,2], Dung Viet Duong[2], Nguyen Dinh Duc[2,*]

[1]*EIVP Ecole des Ingénieurs de la Ville de Paris - Université Gustave Eiffel, 80 Rue Rebeval, 75019 Paris, France*

[2]*VNU University of Engineering and Technology,144 Xuan Thuy, Cau Giay, Hanoi, Vietnam*

Received 21th July 2025
Revised 8th August 2025; Accepted 9th October 2025

**Abstract:** Air pollution in Hanoi represents a pressing public health concern, driven by rapid urbanization and an overwhelming reliance on motorized traffic. This work focuses on evaluating the impact of the Keangnam Hanoi Landmark Tower, standing at 350 meters as Hanoi's tallest structure, on turbulent flows and the dispersion of atmospheric pollutants within a densely populated urban environment. The research employs sophisticated numerical simulations using the Lattice Boltzmann Method (LBM) combined with a block-structured topology-confined mesh refinement approach to model airflow dynamics around the main tower and its two adjacent 212-meter structures. The simulation setup includes a computational domain with defined boundary conditions. Validation with the Kolmogorov scales ensures that the spatial grid size and time step adequately resolves posing the smallest turbulent dissipation scales, confirming the accuracy of the flow and pollutant dispersion patterns. Key findings reveal that recirculation zones and wake vortices trap pollutants in low-velocity areas, elevating local concentrations, and posing respiratory and cardiovascular health risks to residents and pedestrians. Conversely, high-velocity regions around the tower facilitate pollutant dispersion. Moreover, pressure gradients, particularly low-pressure zones in the wake, generate upward suction flows that lift pollutants into higher atmospheric layers, potentially reducing ground-level exposure but increasing concentrations at elevated heights. High-pressure zones on the windward side suppress vertical mixing, further concentrating pollutants near the surface. The study highlights the critical role of urban architectural features in influencing turbulent flow and, by extension, pollution. These insights provide a foundation for developing targeted urban air quality management strategies, such as enhancing natural ventilation, optimizing

* Corresponding author.
*E-mail address:* ducnd@vnu.edu.vn

https//doi.org/10.25073/2588-1124/vnumap.5053

building layouts, and informing health risk assessments to mitigate the socioeconomic impacts of pollution. The research also identifies gaps in current literature on Hanoi's unique urban context and sets the stage for future investigations.

*Keywords:* Turbulent Flow; Pollutant Dispersion; Lattice Boltzmann Method; Vortices; Advection-Diffusion.

## 1. Introduction

Air pollution is a critical global health issue, claiming over 7 million lives annually, with urban areas facing intensified challenges due to high population density and emissions (World Health Organisation, n.d.) [1]. In Hanoi, Vietnam's capital, rapid urban growth and heavy reliance on motorcycles exacerbates pollutant levels, worsened by complex airflow patterns from mixed low and high-rise buildings. This study investigates pollutant dispersion mechanisms in Hanoi's urban environment to understand their health impacts and inform environmental strategies [2]. Hanoi's air quality is severely compromised, with $PM_{2.5}$ levels often exceeding 50 μg/m³, far above the World Health Organisation's 10 μg/m³ guideline, and peaking above 150 μg/m³ in winter due to thermal inversions (European Environment Agency, 2021; World Health Organisation, n.d.) [1, 3]. Nitrogen dioxide ($NO_2$) from the city's 5 million motorcycles, comprising 80% of vehicles, further aggravates pollution, fueled by limited public transport and after the 1990s Đổi Mới urbanization [2, 4]. $PM_{2.5}$ contributes to respiratory and cardiovascular diseases, with a 20% rise in pediatric asthma hospitalizations during high pollution peaks [5]. Economically, pollution increases healthcare costs, reduces productivity, and harms tourism [6]. Government initiatives, like phasing out gasoline motorcycles by 2030, aim to address these issues, underscoring the need for detailed studies on pollution dynamics, which this research explores.

This research investigates the Keangnam Hanoi Landmark Tower, Hanoi's tallest building at 350m , located on Pham Hung Road in Me Tri district of Nam Tu Liem, approximately 7 km west of the city center, within a rapidly developing business hub surrounded by modern buildings. The study focuses on the tower's impact on turbulent flows and pollutant dispersion in a dense urban environment dominated by low-rise structures and varied traffic routes, allowing isolation of its effect on airflow patterns.

As shown in Figure 1 a, the main tower, a 72-story rectangular structure, is constructed with reinforced concrete and a glass façade. Two adjacent 212 m tall (48-story) towers with curved façades, positioned symmetrically 50 m apart, form a triangular layout. Their simplified smooth surfaces and significant height generate complex recirculation zones and wakes, enhancing vertical velocity gradients and pollutant dispersion. The tower's 46 054 m² plot includes gardens that mitigate pollutants but remain exposed to urban emissions [7]. The complex, housing 922 apartments, a 359-room hotel, offices, a mall, and a convention center for over 2,000 people, produces significant pollutants, including fine particulate matter (PM2.5 and PM10), posing health risks [8].

The surrounding area is a dense, active urban zone with high pedestrian activity from employees, shoppers, and tourists, and heavy traffic on major arteries like Pham Hung Road and highway "Ring road 3", intersecting with Me Tri Road, as shown in Figure 1b. These roads, primary pollution sources, experience peak-hour traffic of 10,000–15,000 motorcycles and 1,000–2,000 cars per hour, worsened by congestion near My Dinh bus station. Vehicle emissions generate PM2.5 and PM10 from fuel combustion, brake and tire wear, which linger in the air or settle on surfaces, increasing risks of respiratory and cardiovascular diseases, particularly for the tower's residents due to potential pollutant accumulation from air recirculation [1, 9].

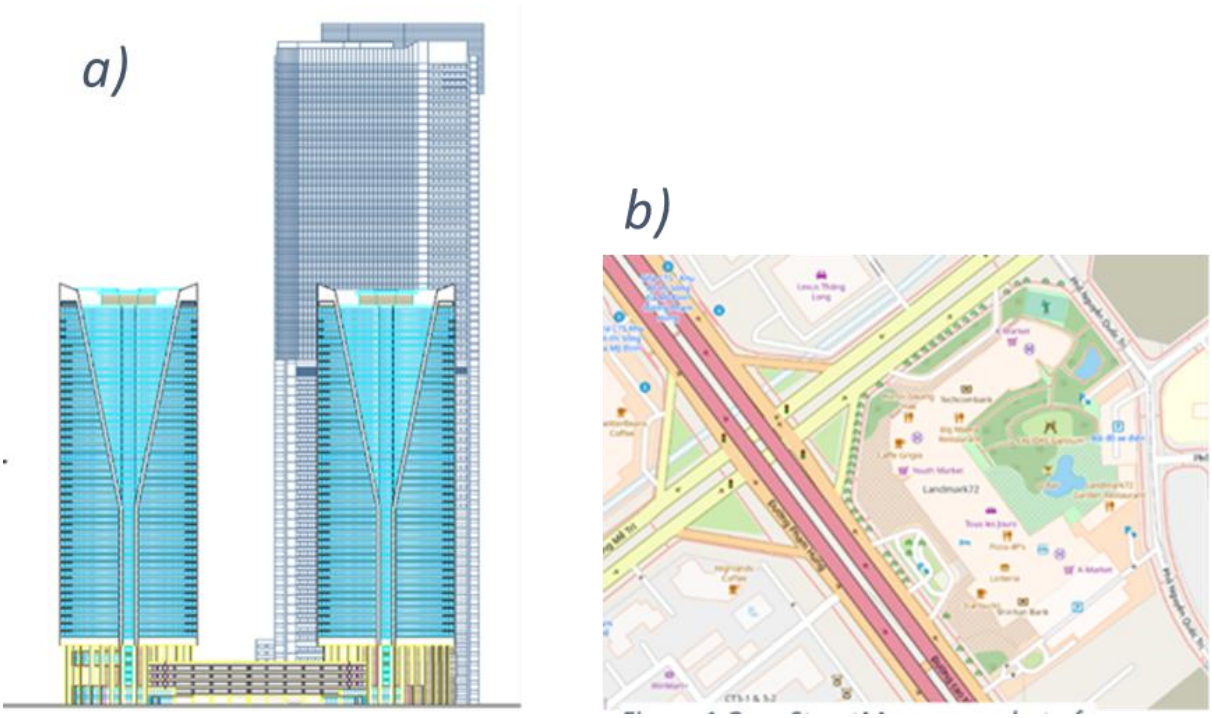


Figure 1. a) AutoCAD architectural plan of the Keangnam Tower;
b) OpenStreetMap extract showing the surroundings of the Keangnam Tower.

The intense traffic provides rich pollutant source data, enabling analysis of high-rise impacts in a dense urban context. The tower's prominence facilitates access to architectural and environmental data, supporting numerical modeling and comparisons with global high-rise studies, validating results, and highlighting Hanoi's unique pollution challenges. The dense population around the tower underscores the study's relevance to public health and resident well-being. Research on urban turbulent flows and pollutant dispersion is expanding due to urban challenges. Studies like [9] demonstrate that urban canyons create recirculation zones, trapping pollutants and elevating health risks. Blocken et al., [10] employs computational fluid dynamics to emphasize urban geometry's role in ventilation and dispersion. Tominaga et al., [11] model flows in dense urban settings, often using simplified geometries to capture flow dynamics. Hanoi's unique context marked by rapid urbanization and motorcycle-driven pollution remains understudied. This study on the Keangnam Landmark Tower investigates a real structure's impact on pollutant dispersion, identifying dynamic phenomena like recirculation zones to inform air quality management [12]. Additional global studies enrich this analysis: Lateb et al., [13] uses computational fluid dynamics to model pollutant dispersion around buildings, emphasizing recirculation zones; Mei et al., [14] employs large-eddy simulation to study turbulent structures and pollutant trapping in urban wakes; Aristodemou et al., [15] investigates computational fluid dynamics modeling of pollutant dispersion in urban street canyons; Peng et al., [16] explores turbulent flow and pollutant dispersion for urban ventilation in a thesis. By focusing on Hanoi, where pollution exceeds standards, it addresses a literature gap, providing insights for local ventilation strategies and broader urban applications).

To analyze the influence of the Keangnam Landmark Tower on the dispersion of air pollutants in Hanoi, it is essential to understand how the air behaves around urban structures. This behavior is

governed by the principles of fluid mechanics, a discipline that studies the movements of gases and liquids. A clear and accessible presentation of these concepts is therefore essential to lay the foundations of this study and explain the complex phenomena that will be modelled numerically.

When air circulates freely, it can adopt a laminar flow, characterized by regular and orderly trajectories. However, an imposing tower like the Keangnam disturbs this flow. The air becomes turbulent, creating phenomena such as vortices of air and recirculation zones, where the air rotates on itself. These disturbances can trap pollutants, such as fine particles or toxic gases, affecting nearby air quality.

To analyze and predict these complex flow patterns, the Navier-Stokes equations are utilized. These mathematical expressions describe how air's velocity, pressure, and viscosity govern its motion. In a complex urban environment like Hanoi, these equations are only solvable using Computational Fluid Dynamics (CFD). This method discretizes the space around the Keangnam Landmark Tower into small elements to numerically simulate turbulence, vortices, and recirculation zones, providing a precise visualization of airflow dynamics.

This study uses these principles to model turbulent flows around the Keangnam Landmark Tower and analyze their impact on pollutant dispersion. The question that guides this work is the following: how can the numerical modeling of the turbulent flows around this tower contribute to understanding the dispersion of air pollutants and to propose solutions to improve air quality in Hanoi?

To guide our study on pollutant dispersion around the Keangnam Landmark Tower, we predict that air velocity around the tower directly influences pollutant particle distribution. Like a river carrying leaves, fast-moving air disperses pollutants such as fine dust or gases over greater distances, while slower air or vortices near the tower cause particles to accumulate, increasing local pollution. Using numerical simulations based on the Navier-Stokes equations, we will track particle movement in the airflow. By analyzing air velocity at various points, such as near the ground, along walls, or in vortex zones, we will estimate where pollutants concentrate or disperse, employing the dispersion equation to link particle concentration to fluid velocity.

The rest of this article details the methodology, including Lattice Boltzmann equations, the description of the simulation and the numerical set up. The study proceeds with the results, their validation using Kolmogorov scales, and a comparison with existing work to evaluate the contributions and impact of our research on understanding pollutant dispersion in an urban environment like Hanoï.

## 2. Methodology

### *2.1. Multiple-relaxation-time Lattice Boltzmann Equation*

This present study uses an indoor code based on the mesoscopic approach known as the lattice Boltzmann equation (LBE). The LBE is a powerful numerical method used in computational fluid dynamics (CFD) for turbulence, heat, multi-component and micro-flow applications [17]. In contrast to typical CFD approaches [18-20], the Navier–Stokes equations (NSE) in the hydrodynamic limit are recovered using discretized particle distribution functions $\Gamma$ [21]. The LBE reconstructs the physical dynamics of viscous flows. By using the Bhatnagar–Gross–Krook (BGK) collision model [22, 23], the LBE can be written as :

$$\Gamma_i(x + e_i\Delta t, t + \Delta t) = \Gamma_i(x, t) - \omega\left(\Gamma_i(x, t) - \Gamma_i^{eq}(x, t)\right) \tag{2.1}$$

Where $\Gamma_i$, $\Gamma_i^{eq}$, $x$, $e_i$, $\Delta t$ and $\omega = 1/\tau$ are the discrete-velocity distribution function, the local equilibrium distribution function, the corresponding physical location in space, particle velocity in the

i-th direction, time streaming step and relaxation frequency with a single relaxation time τ. A general LBE procedure is divided into collision and streaming. While the collision process performs the right-hand side of (2.1), the streaming process accomplishes the full (2.1). In the current work, the D3Q27 (27 discrete velocities in 3 dimensions) particle velocity model is used; because it has been demonstrated that the LBE may meet the rotationally invariant flow condition in turbulence [24]. The expression for this discretized velocity set is

$$e_i = \begin{cases} 0, & \mathrm{i} = 0; \\ (\pm 1,0,0),(0,\pm 1,0),(0,0,\pm 1)\mathrm{c}, & \mathrm{i} = 1,2,3,4,5,6; \\ (\pm 1,\pm 1,0),(\pm 1,0,\pm 1),(0,\pm 1,\pm 1)\mathrm{c}, & \mathrm{i} = 7,8,\ldots,17,18; \\ (\pm 1,\pm 1,\pm 1)\mathrm{c}, & \mathrm{i} = 19,20,\ldots,25,26, \end{cases} \tag{2.2}$$

here, $c = \frac{\Delta x}{\Delta t}$ is taken as 1 where $\Delta x$ is the lattice spacing. For the D3Q27 model, the second-order local equilibrium distribution function is parametrized by the local values of density $\rho$ and flow velocity $u$

$$\Gamma_i^{eq}(x,t) = \rho\, w_i \left[ 1 + \frac{e_i \cdot u}{c_s^2} + \frac{(e_i \cdot u)^2 - (c_s|u|)^2}{2\, c_s^4} \right] \tag{2.3}$$

Where $w_0 = \frac{8}{27}$ , $w_i = \frac{2}{27}$ for $i = 1-6$, $w_i = \frac{1}{54}$, for $i = 7-18$, $w_i = \frac{1}{216}$, for $i = 19-26$, and $c_s = \frac{c}{\sqrt{3}}$ Using the Chapman–Enskog analysis, the kinematic viscosity ν is associated with the single relaxation time τ as a connection between the LBE and the NSE (Huang, 2008) [25], $\nu = c_s^2(\tau - 0.5\,\Delta t)$ As a result, the results obtained from LBE can reveal values in macroscopic behaviour. However, the numerical stability of the BGK operator is limited when the value of the kinematic viscosity is sufficiently small. This issue often occurs in grid refinement attempts (discussed in the next section), cutting the single relaxation time (Wang, 2020) [26]. Based on the collision procedure (Lallemand & Luo, 2000) [27], the multiple-relaxation-time (MRT) LBE is therefore performed to raise the free parameters of the relaxation time. In particular, the particle population relaxes in moment space instead of normal velocity space. Hence, (2.1) is replaced by:

$$\Gamma_i(x + e_i\Delta t, t + \Delta t) = \Gamma_i(x,t) - M^{-1}S\left[m_i(x,t) - m_i^{eq}(x,t)\right]\Delta t, \tag{2.4}$$

where $M$, $S$ and $m_i$ are the transformation matrix, collision matrix and moment space for distribution function $\Gamma$ , respectively. In the current study, the matrices $M\ and\ S$ are chosen from the results of the study of Suga et al. [24] for turbulent flow. In particular, $S$ is a 27×27 diagonal matrix with $s_{0-3} = 0$, $s_4 = 1.54$, $s_{5-9} = \frac{1}{0.5 + 3\nu}$, $s_{10-12} = 1.5$, $s_{13-15} = 1.83$, $s_{16} = 1.4$, $s_{17} = 1.61$, $s_{18-22} = 1.98\ and\ s_{23-26} = 1.74$. The formulation of transformation matrix $M$ is established through the analysis of (Dubois & Lallemand, 2011) [28]. A detailed performance of matrix $M$ can be observed in Suga's study. All processes in the MRT method greatly improve the accuracy and stability of the single-relaxation-time lattice Boltzmann model.

Finally, macroscopic flow quantities (mass density $\rho$, flow velocity $u$ and intrinsic average pressure $p$) in the LBE framework can be obtained from moments of the particle distribution function

$$\boldsymbol{\rho(x,t)} = \sum_i \boldsymbol{\Gamma_i(x,t)}, \qquad \boldsymbol{\rho u(x,t)} = \sum_i \boldsymbol{e_i \Gamma_i(x,t)}, \qquad \boldsymbol{p(x,t) = \rho(x,t) c_s^2} \tag{2.5}$$

### *2.2. Boundary Condition for Bounded Flo*

In order to define the presence of rigid bodies in the fluid field, the input geometry uses the standard triangle language data, which provide the normal vector and vertex coordinates of triangular facets,

defining the body surface as shown in Fig. 2a. On the Cartesian mesh as depicted in Fig. 2b, three types of cells are determined, including solid cells $x_s$, boundary cells $x_b$ and fluid cells $x_f$. Initially, the type of fluid cell is put in the full computational domain. The solid cells are then found using a fast ray-triangle intersection algorithm proposed by (Möller & Trumbore, 2005) [29]. Specifically, the exploration of solid cells is an inside/outside check of fluid cells with all triangular facets based on the ray parameterization. Then, the boundary cells $x_b$ are the cells between the fluid cell and the solid cell. Finally, Fig. 2c) demonstrates the three cell types after performing the ray-triangle intersection algorithm. At the boundary cell, the streaming

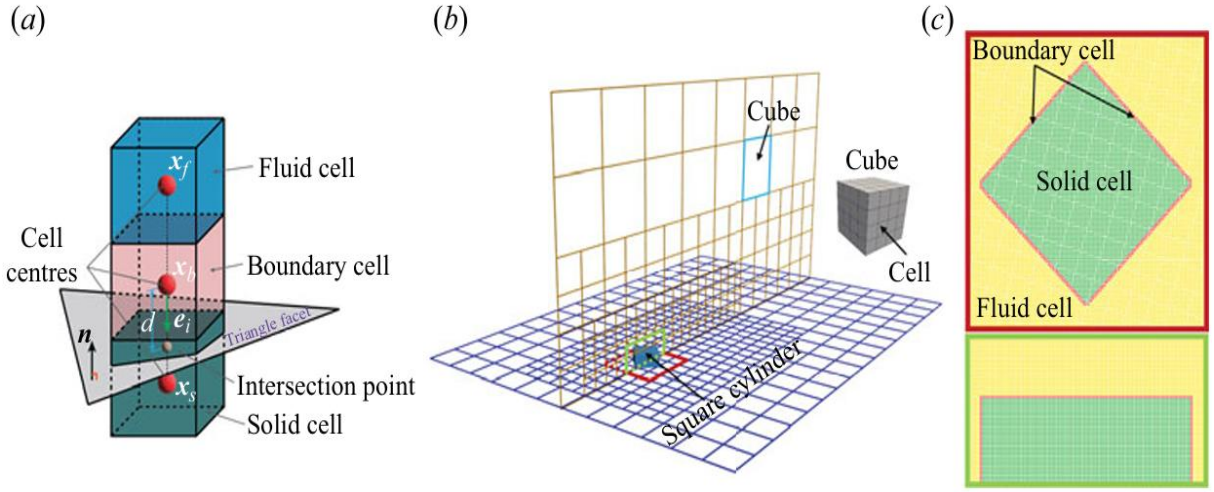


Figure 2. Interpolated bounce-back boundary condition (a); topology-confined block refinement with three levels (b); three partitions of solid cell, boundary cell and fluid cell (c) [23].

The process is performed to consider the intentional neglect of lattice directions prevented by solid cells. This omission is compensated by the interpolated bounce-back (IBB) method that satisfies the flow behaviour of second-order accuracy on the curved wall surface. The basic idea of the IBB method is to store the information of the intersection point between particle velocity vector $e_i$ and the triangle facet. Determining the point of intersection is also performed by the ray-triangle intersection algorithm. According to (Bouzidi et al. 2001) [30], the reflection of a distribution function is predicted by linear interpolation. The a priori unknown bounced-back population is constructed from known populations at $x_b$ and $x_f$ as

$$\Gamma_{\bar{i}}(x_b, t+\Delta t) = \begin{cases} 2\mathrm{q}\Gamma_i^+(\mathrm{x_b},\mathrm{t}) + (1-2\mathrm{q})\Gamma_i^+(\mathrm{x_f},\mathrm{t}), & \mathrm{q} \le \dfrac{1}{2}, \\ \dfrac{1}{2q}\Gamma_i^+(\mathrm{x_b},\mathrm{t})\dfrac{2\mathrm{q}-1}{2\mathrm{q}}\Gamma_{\bar{i}}^+(\mathrm{x_b},\mathrm{t}), & \mathrm{q} \ge \dfrac{1}{2}, \end{cases} \tag{2.6}$$

where q is the distance ratio between the distance measured from the boundary cell $x_b$ to the intersection point and the magnitude of the discrete velocity vector $e_i$. As a result, $q = \frac{d}{|e_i|\Delta t} \in [0,1]$ Represents the reduced wall location information. Total fluid forces acting on the three-dimensional rigid body's surface F ($F_x$, $F_y$, $F_z$) are computed by the momentum exchange method (Chen et al., 2013) [31] on the boundary cell layer.

### *2.3. Topology-confined Block Refinement*

Based on the block-structured grids of Duong et al., [32], a framework of topology-confined block refinement is developed, as shown in Fig. 2b. The computational domain is partitioned into areas of different grid sizes, called cube-shaped blocks. This spatial difference is characterized by an indicator called refinement level l. Therefore, the mesh system is constructed with the value $l$ ranging from 0 to $l = m - 1$, where $m$ is the number of the expected refinement level. The refinement level $l$ increases from the confined flow region near the solid bodies to far-field regions. In each block, the uniform Cartesian grid (cells) is used to store and solve the variables in the LBE. The efficiency and robustness of the management of the informational communication between refined and unrefined blocks are demonstrated in the numerical studies of Kematsuchi [33] and Ishida et al., [34]. In each block, the index, coordinates, spatial size, cell number, grid refinement level, and neighboring block information are stored to provide detailed instructions within the cache environment for parallel computing. For parallelism, the block distribution on each grid refinement level is performed by a load-balanced linear distribution algorithm based on the space-filling curve theory [35]. This procedure is implemented with the message passing interface technique, which is specially designed to function on parallel computing architectures. After distributing block data to each node, independent workloads are numerically performed by open multi-processing thread parallelization. Due to the space limitation, the interested readers are referred to the work of Duong et al., [32] for the detailed algorithm of topology-confined block refinement.

## 3. Numerical Set - up

### *3.1. Numerical Model and Computational Domain*

A numerical model of the Keangnam Hanoi Landmark Tower and its two adjacent towers is constructed, as shown in Fig. 2a. The model dimensions are defined with the main tower having a rectangular footprint of 93 m × 57 m, while each adjacent tower is approximated with a triangular base with sides measuring 53 m. Each tower features curved façades. The height of the main tower is set to 350 m, and the height of each adjacent tower is set to 212 m. The towers are modeled as rigid structures fixed to the ground plane with smooth surfaces, neglecting details such as balconies, decorations, or surrounding low-rise buildings to simplify the mesh and reduce computational complexity. The model is created using SALOME software from AutoCAD architectural drawings, as shown in Figure 3a, ensuring accurate representation of the towers' layout and dimensions compatible with the meshing method.

The width ($D$) is used to normalize length scales and dimensions here, $D = 93\,m$ . The height of the tower is then $H = 350\,m = 3{,}76\,D$ . Figure 3a show the schematic of the computational domain and the definition of the coordinate system with the streamwise (x), spanwise (y) and vertical (z) dimensions illustrated by the red, dark blue and green arrows. In Figure 3b the computational domain size is selected as $22D$ on X so the lateral length is larger than the recommended value reported as at least $10D$ for the sufficient accuracy by Tamura et al., [36], thus ensuring the adequate lateral length. $12D$ on Y and $10D$ on Z because Cao et al., [37] has proposed the minimum height $10D$ of the top boundary Therefore, in the present study, due to the setup of uniform inflow (no turbulent boundary layer at the inlet), the vertical length of $10D$ is sufficiently large to capture the flow physics. The characteristic lengths of the tower are presented on the normalized length scale. Figure 3c presents the characteristic lengths on the plan Y-Z at $X = 22D$. Figure 3d presents the characteristic lengths on the plan X-Z at $Y = 0D$. Figure 3e presents the characteristic lengths on the plan X-Y at $Z = 10D$

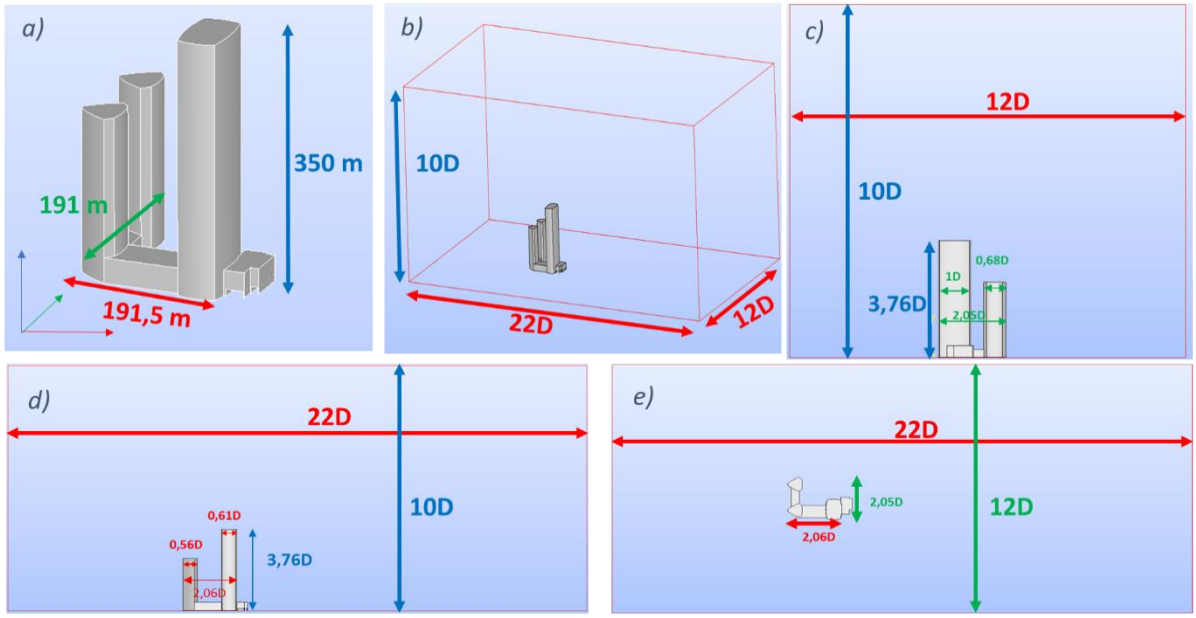


Figure 3. a) Keangnam Landmark Tower's 3D model on SALOME and characteristic lengths; b) 3D representation of the computational domain; c) Characteristic lengths of the tower on plan Y-Z at $\boldsymbol{X = 22D}$; d) Characteristic lengths of the tower on plan X-Z at $\boldsymbol{Y = 0D}$; e) Characteristic lengths of the tower on plan X-Y at $\boldsymbol{Z = 10D}$.

### *3.2. Simulation Input Data*

The boundary conditions for the simulation are defined as follows. A uniform free-stream velocity is set at the inlet boundary, calculated based on the Reynolds number to represent turbulent flow conditions. The air properties at room temperature are used: Density ($\rho = 1.225, \mathrm{kg/m^3}$) and kinematic viscosity ($\nu = 1.5 \times 10^{-5}\ \mathrm{m^2/s}$), consistent with an incompressible fluid assumption of Shu et al., [38]. The Reynolds number, characterizing the turbulent flow regime, is set to $Re = 6{,}000{,}000$. From $Re$, we can deduce the wind speed ($U$) by $\left[U = \frac{Re\nu}{L}\right]$ giving a speed of $0.9677\ m/s$ with ($L$), the characteristic length is $L = 93\ m$. This represents a light wind, limiting pollutant dispersion and simulating a worst-case scenario where pollutants tend to stagnate.

The wind direction is set perpendicular to the widest face ($L = 93\ m$) of the main tower to maximize turbulence and eddy formation, improving the accuracy of modeling recirculation [11, 39, 40]. Free-slip boundary conditions are applied to the lateral and upper boundaries of the computational domain to minimize artificial shear stress [41, 42]. The uniform free-stream velocity is set as U∞ at the inlet boundary and an open boundary condition, defined by ($\partial \mathrm{u}/\partial \mathrm{x} = 0$), is used at the outlet boundary to allow flow to exit without reflection. No-slip boundary conditions are applied on the ground surface using the half-way bounce-back method [43]. No-slip boundary conditions are modeled on the surfaces of the main and adjacent towers using the Immersed Boundary Method (IBB).

### *3.3. Block Distribution*

A refined cell distribution is implemented in a localized region where the boundary layer forms. Fig. 4 illustrates three refinement levels, denoted as $m = 3$, with cell sizes of Δ, 2Δ, 4Δ, corresponding to levels $l = 0, 1, 2$ respectively. The finest resolution, level $l = 0$, is configured to encompass the

separated shear layers developing on the top and side surfaces of the square cylinder. The grid generation approach involves three steps: selecting the block refinement level, specifying the dimensions of blocks with equivalent refinement within the computational domain, and defining a uniform cell size, with cells evenly distributed in all three directions of each cubic block. The total grid count is calculated by multiplying the number of blocks by the number of cells per block. To establish the minimum cell size, the boundary layer thickness ($\delta_B$) on the cylinder's surfaces is computed using the formula $\delta_B = (5.5 \cdot 0.5w)/\sqrt{Re_{0.5w}}$ as described by White [44]. This allows fine turbulence structures to be captured efficiently without refining the entire domain, balancing accuracy and computational cost [31]. The total number of cells is detailed in Table 1 and it directly affects computation time, memory usage, and overall simulation feasibility [42].

Table 1. Grid size table showing the grid levels used and the corresponding number of cells at each level

| Level | Lv. 0 | Lv.1 | LV.2 | Total |
|---|---|---|---|---|
| D | 20.0 | 40.0 | 80.0 | |
| K. viscosity | 0.00400 | 0.00800 | 0.01600 | |
| Block | 168 | 892 | 3232 | 4292 |
| Cell | 10,752,000 | 57,088,000 | 206,848,000 | 274,688,000 |

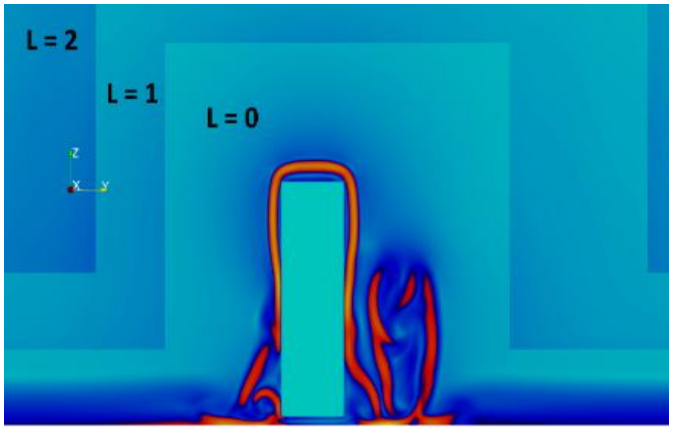


Figure 4. Paraview visualization of the three refinement levels.

### *3.4. Verification by Kolmogorov Scale*

The initial simulation is validated by comparing the spatial grid size (Δx) and time step ($\Delta t$) with the Kolmogorov scales, which define the smallest length and time scales of turbulent energy dissipation [45, 46]. Turbulence encompasses a broad spectrum of flow scales, ranging from large eddies influenced by the geometry to small scales dominated by viscous effects. Kolmogorov's statistical framework for high-Reynolds-number turbulence describes the cascade of kinetic energy from large to small eddies, where it is ultimately dissipated by viscosity. The Kolmogorov scales, representing the threshold where viscous dissipation balances energy transfer, are determined solely by the kinematic viscosity (ν) and the energy dissipation rate (ϵ). with $\eta = (\nu^3/\epsilon)^{1/4}$, $\tau = (\nu/\epsilon)^{1/2}$ and $\epsilon = (\nu/2)\overline{\left(\partial u_i'/\partial x_j^* + \partial u_j'/\partial x_i^*\right)^2}$

The Kolmogorov scales serve as criteria for the spatial grid size ($\Delta x$) that must resolve all the eddies, and the time step ($\Delta t$) that must be sufficiently small to capture the fastest turbulent fluctuations. Those

criteria are: ($\Delta x \leq C\eta$) and ($\Delta t \leq C\tau$). Yakhot et al. [47] highlighted that the ratio of ($\Delta x/\eta$) should be less than 5 in the critical regions and ($\Delta t/\tau$) less than 1.

To ensure an exhaustive analysis of the space, we have chosen to discretize the domain into 5 planes along each axis in Fig. 5, i.e. a total of 15 sections. On each of these brackets, we compare our conditions. The results of this verification are presented in Table 2 and on some Paraview slice of ($\Delta x$ /η) and ($\Delta t/\tau$) values on the X2, Y4, and Z3 planes Figure 6.

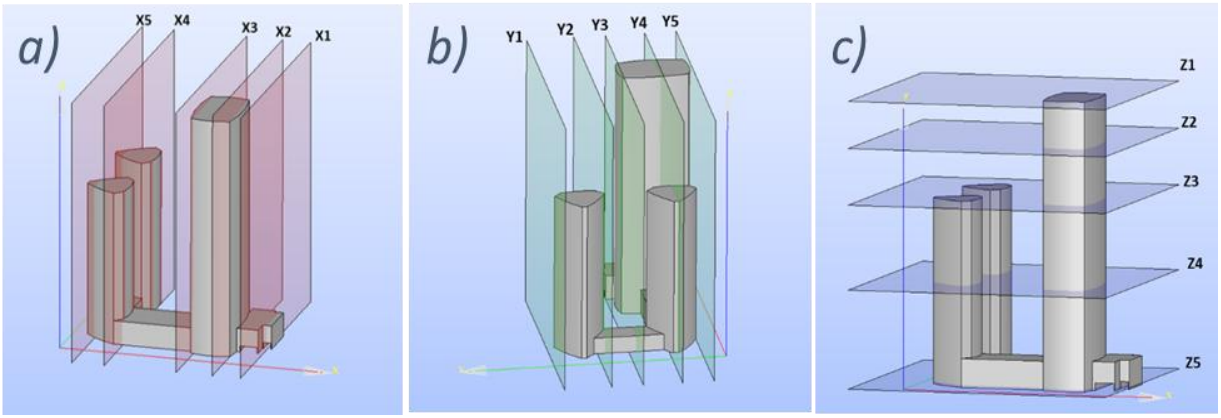


Figure 5. a) Discretization of the 3D model along the X-axis b) Discretization of the 3D model along the Y-axis c) Discretization of the 3D model along the Z-axis.

Table 2. Verification of the ratio $\boldsymbol{\Delta x/\eta < 5}$ and $\boldsymbol{\Delta t/\tau < 1}$ for each plane

| | **Coordinates** | **Grid size/ Kolmogorv length scale** | | **Time step / Kolmogorov time scale** | |
|---|---|---|---|---|---|
| | **Plan** | **Max** | **Threshold** | **Max** | **Threshold** |
| **Normal to Y** | Plan Y1 | 2 | <5 | 0.063 | <1 |
| | Plan Y2 | 2 | <5 | 0.063 | <1 |
| | Plan Y3 | 2 | <5 | 0.063 | <1 |
| | Plan Y4 | 2 | <5 | 0.063 | <1 |
| | Plan Y5 | 2 | <5 | 0.063 | <1 |
| **Normal to X** | Plan X1 | 1.1 | <5 | 0.02 | <1 |
| | Plan X2 | 1.3 | <5 | 0.026 | <1 |
| | Plan X3 | 1.4 | <5 | 0.029 | <1 |
| | Plan X4 | 1.5 | <5 | 0.036 | <1 |
| | Plan X5 | 1.4 | <5 | 0.029 | <1 |
| **Normal to Z** | Plan Z1 | 1.8 | <5 | 0.054 | <1 |
| | Plan Z2 | 1.8 | <5 | 0.053 | <1 |
| | Plan Z3 | 1.6 | <5 | 0.043 | <1 |
| | Plan Z4 | 1.7 | <5 | 0.044 | <1 |
| | Plan Z5 | 1.5 | <5 | 0.034 | <1 |

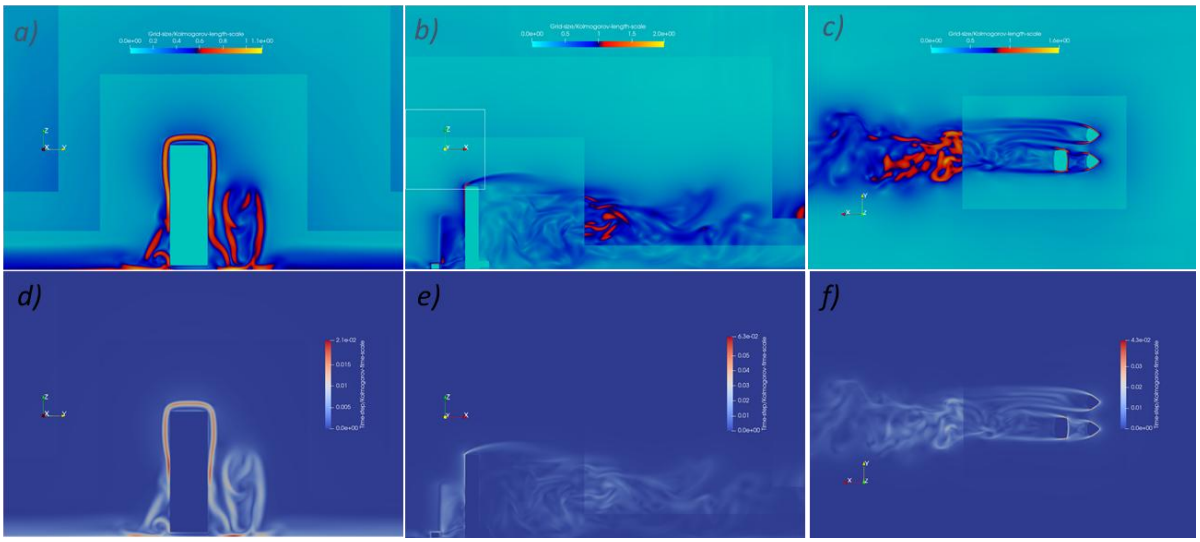


Figure 6. a) Paraview ($\boldsymbol{\Delta x}$ /η) values on the X2 plane;b) Paraview ($\boldsymbol{\Delta x}$ /η) values on the Y4 plane; c) Paraview ($\boldsymbol{\Delta x}$ /η) values on the Z3 plane; d) Paraview ($\boldsymbol{\Delta t/\tau}$) values on the X2 plane; e) Paraview ($\boldsymbol{\Delta t/\tau}$) values on the Y4 plane f) Paraview ($\boldsymbol{\Delta t/\tau}$) values on the Z3 plane.

This shows that our time step and grid size are sufficiently small in order to capture the turbulent fluctuations in the present numerical simulations.

## 4. Results

### *4.1. The Velocity Field*

To determine the location and quantity of pollutants, the most effective approach is to examine their concentration. In our case, the optimal method for assessing concentration is to employ the advection-diffusion equation, which provides a robust framework for capturing the transport and dispersion processes. This section will therefore present the analysis of the simulation outcomes, with a primary focus on the velocity field. The velocity distribution will be utilized to infer the concentration of pollutants, providing insights into the dispersion patterns within the computational domain (Malik et al., 2024) [48]. The advection-diffusion equation is:

$$\frac{\partial C}{\partial t} + \mathrm{u} \cdot \nabla C = \nabla \cdot (D \nabla C) + S \tag{4.1}$$

with $\frac{\partial C}{\partial t}$ representing the rate of change of concentration over time, $\mathrm{u} \cdot \nabla C$ the advection driven by the velocity field, $\nabla \cdot (D \nabla C)$ the diffusion due to the diffusion coefficient, and $S$ the source.

We make the assumptions of a constant incoming wind and a constant pollution source meaning that $\frac{\partial C}{\partial t} = 0$ [49], so we can simplify the advection-diffusion equation by:

$$u \cdot \nabla C = \nabla \cdot (D \nabla C) + S \tag{4.2}$$

The Peclet number ($Pe = \frac{|u|L}{D}$) (with $L = 93$), serves as an indicator of the relative dominance of advection over diffusion. A value of ($Pe \gg 1$), signifies that the advective transport significantly

outweighs diffusive processes, implying a predominant role of wind in dispersing pollutant particles compared to natural diffusion.

As a reminder, the wind speed at the source is ($u = 0.9677\ m/s$) and it varies from ($u = 0\,m/s$) to ($u = 5\,m/s$) in the simulation, as shown in

Figure 7. The diffusion coefficient D, representing the turbulent mixing of pollutants in urban environments, is estimated to range between $D = 10^{-2}$ and $D = 10^{-1}\ \mathrm{m}^2/\mathrm{s}$ supported by (Batchvarova & Gryning, 2006; Venkatram et al., 2002) [50, 51].

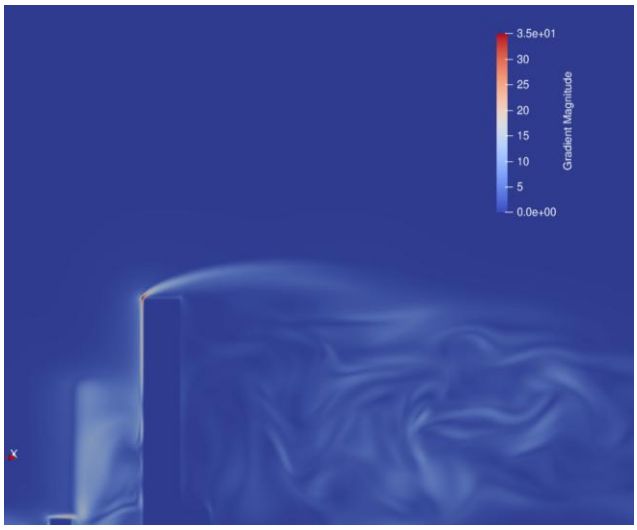


Figure 7. Wind speed Y4 plane.

This gives us a $Pe$ range from : $Pe = 900$ for ($u = 0.9677\,m/s$ and ($D = 10^{-1}\ \mathrm{m}^2/\mathrm{s}$) to $Pe = 42500$ for ($u = 5\,m/s$ and ($D = 10^{-2}\ \mathrm{m}^2/\mathrm{s}$). In any case, we have $Pe \gg 1$.

We employ a "Paraview" to visualize the streamlines of the velocity field, which represent the instantaneous paths of fluid particles. These streamlines serve as a reliable proxy for the pollutant concentration field, as indicated by the high Peclet number (Pe $\gg$ 1).

The connection between velocity and concentration has been extensively explored in scientific studies. Britter & Hanna [52] noted that in urban environments, pollutant transport aligns with flow streamlines. Similarly, Venkatram et al., [51] demonstrated through urban tracer experiments that concentrations closely follow the velocity field's paths. The paraview visualization of the velocity field on Figure 8-10 clearly highlights the turbulent flow patterns triggered by the presence of the tower. This turbulent flow is characterized by reduced velocities and the formation of large-scale vortices, which show significant differences across various planes. These vortices, distinguished by their low-speed central regions, play a critical role in capturing and retaining pollutants. As wind flows past the tower, it encounters the structure's bluff shape, leading to flow separation and the creation of recirculation zones. These zones, marked by slower flow speeds and rotational motion, act as traps for pollutants, causing a noticeable increase in local concentrations. The vortices stem from the tower's bluff geometry, with their low-speed cores functioning as stagnation areas that hinder the downstream movement of pollutants.

This trapping effect is well-supported by existing research. Lim et al., [53] have shown that pollutants are retained within the near-wake vortices behind structures, while Hertwig et al., [54] emphasize how slow-moving vortices effectively hold onto airborne particles. In the tower's wake, these

vortices ensnare pollutant particles, resulting in higher concentrations within their low-speed interiors. The combination of rotational motion and diminished flow velocities generates stagnation zones that restrict advective transport, the process by which pollutants are carried away by the flow, leading to their accumulation. This process notably elevates the local levels of fine particulate matter, such as PM2.5, which remains suspended within the vortex cores for extended periods. Recent investigations reinforce this pattern: Rich & Vanderwel [55] used scale model experiments to show that the horseshoe vortex surrounds tall structure traps pollutants, raising concentrations near the ground. Similarly, Fu et al., [56] employed large-eddy simulation to demonstrate that recirculation vortices behind groups of buildings retain pollutants, shaping their dispersion behaviour across urban landscapes.

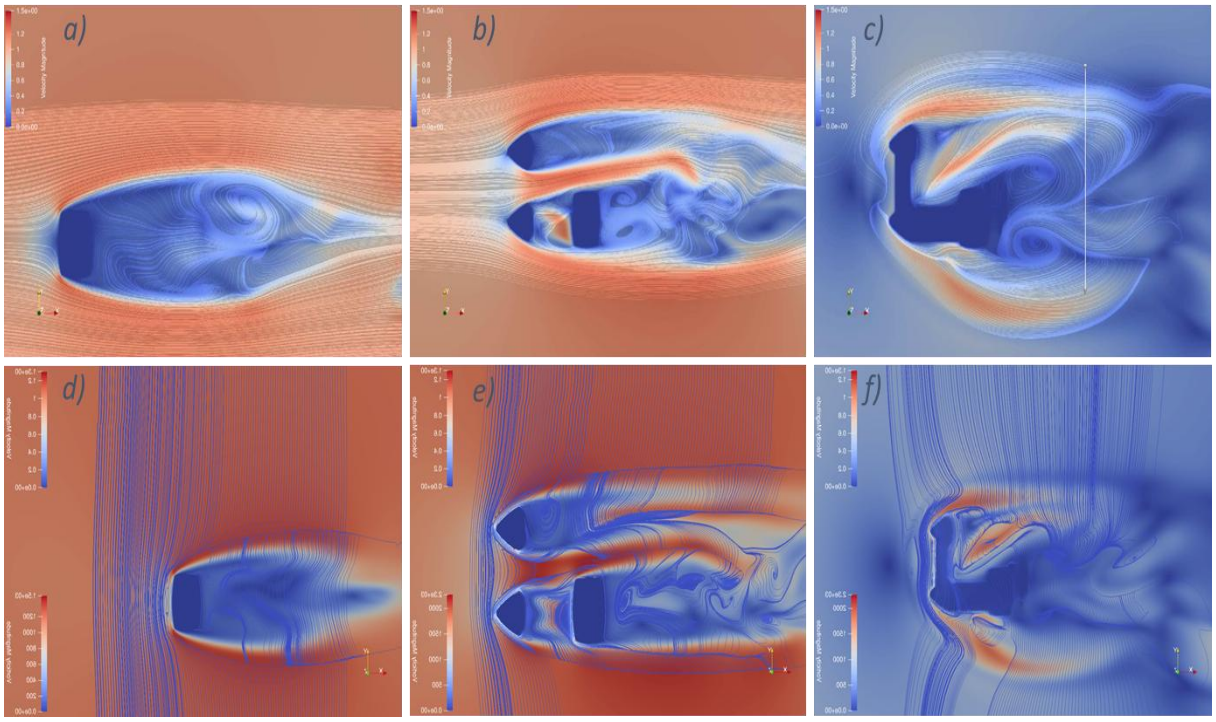


Figure 8. a) Paraview velocity streamlines on plane Z1; b) Paraview velocity streamlines on plane Z3; c) Paraview velocity streamlines on plane Z5; d) Paraview vorticity streamlines on plane Z1; e) Paraview vorticity streamlines on plane Z3; f) Paraview vorticity streamlines on plane Z5.

Vorticity, defined as a measure of the flow's rotational strength ($\omega = \nabla \times u$) (Figure 8-10), also plays a significant role in determining pollutant concentration. Elevated vorticity levels within the vortex cores strengthen the rotational motion, creating regions where pollutants are confined and their concentrations increase over time. This heightened rotational intensity limits mixing with surrounding air streams, allowing pollutants to build up within these zones. The effect becomes especially prominent in the wake of the tower, where vorticity helps maintain the stability of these rotating structures, further enhancing pollutant retention. This dynamic is corroborated by Moeng & Rotunno [57], who highlight that vorticity-driven eddies improve the confinement of scalars like pollutants, and Kida & Miura [58], who confirm that high-vorticity areas link to increased pollutant concentrations due to prolonged trapping.

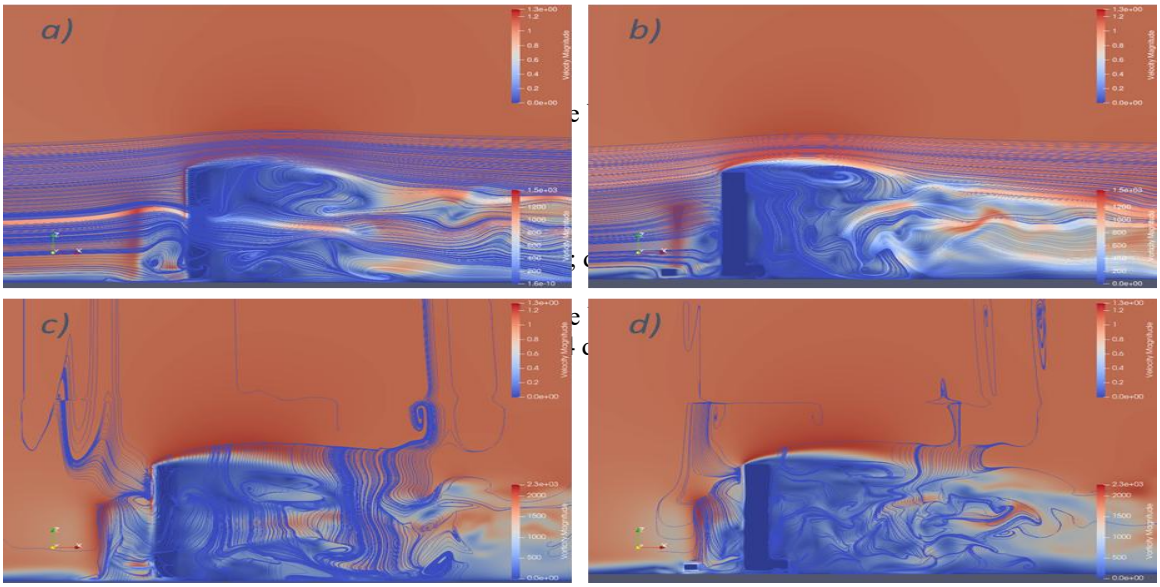


Figure 9. a) Paraview velocity streamlines on plane Y4; b) Paraview velocity streamlines on plane Y5; c) Paraview vorticity streamlines on plane Y4 d) Paraview vorticity streamlines on plane Y5.

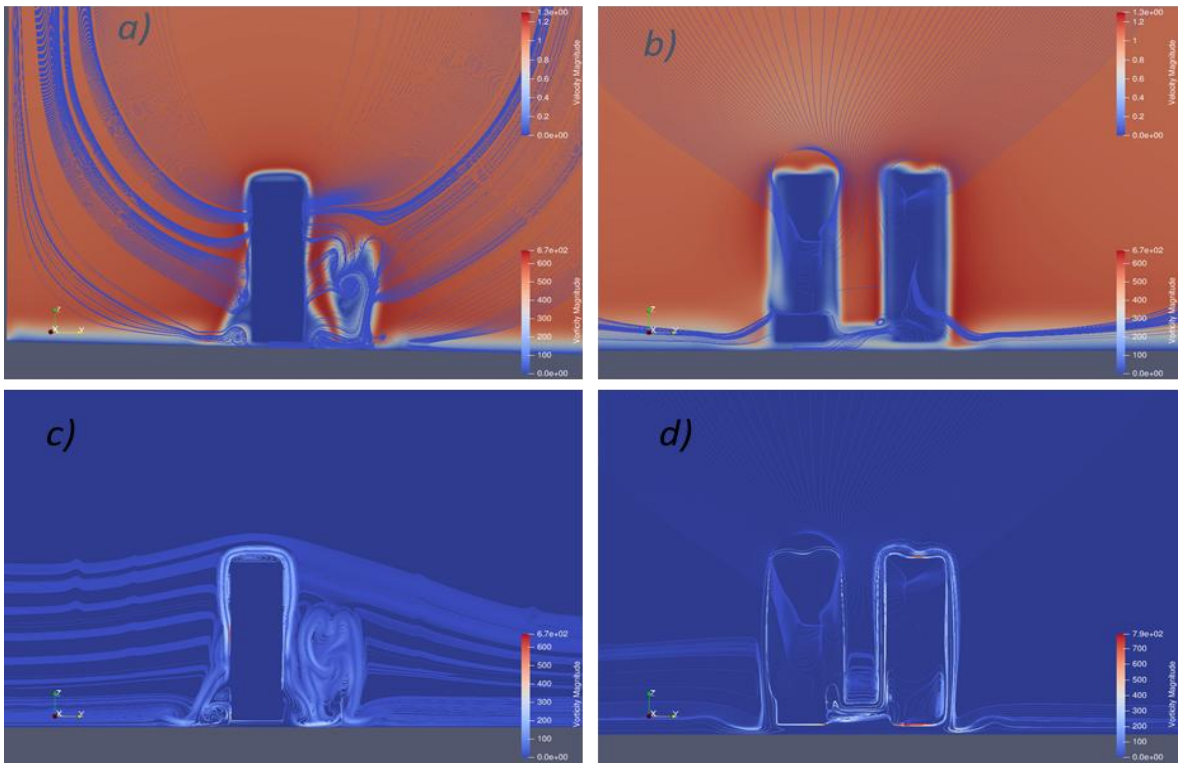


Figure 10. Paraview velocity streamlines on plane X2; b) Paraview velocity streamlines on plane X4; c) Paraview vorticity streamlines on plane X2; d) Paraview vorticity streamlines on plane X4.

### 4.2. The Pressure Field

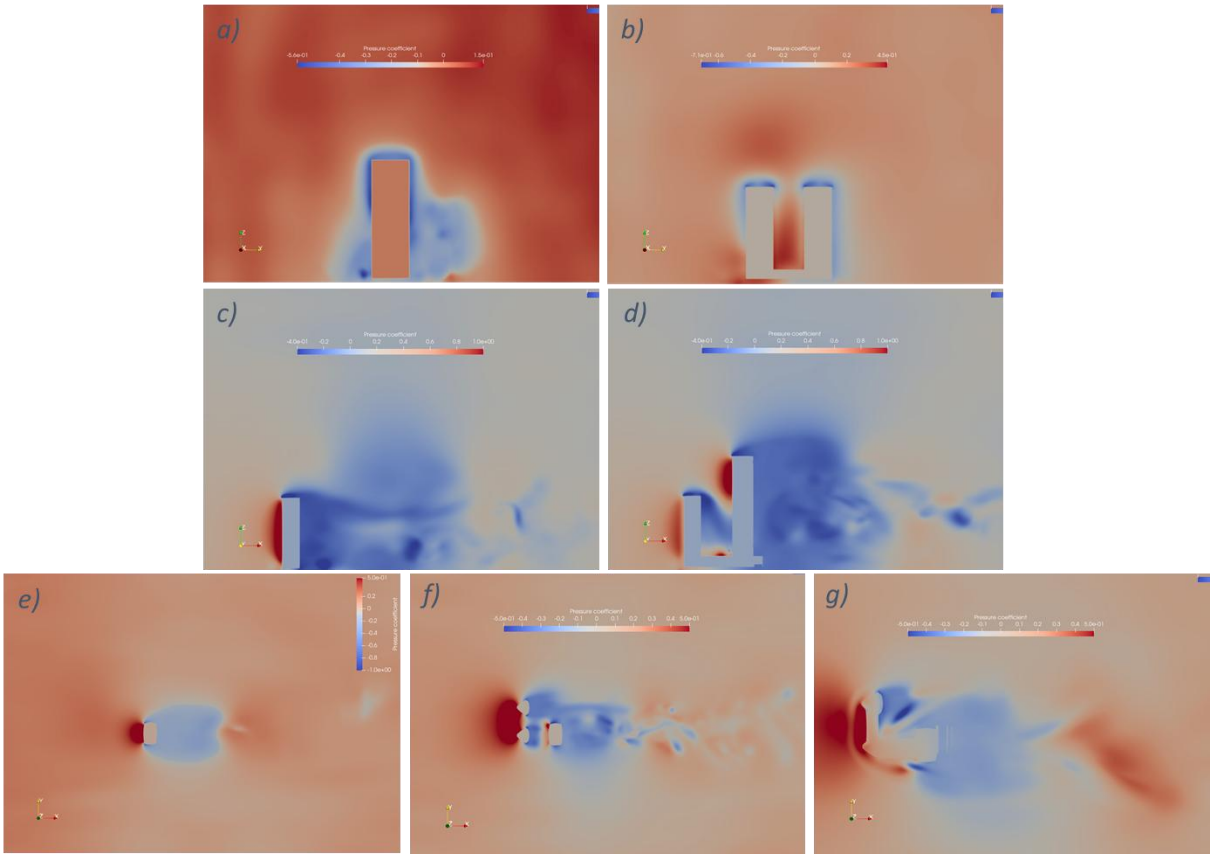


Figure 11. a) Paraview pressure field on plane X3; b) Paraview pressure field on plane X4; c) Paraview pressure field on plane Y2; d) Paraview pressure field on plane Y4; e) Paraview pressure field on plane Z1; f) Paraview pressure field on plane Z3; g) Paraview pressure field on plane Z5.

The pressure field surrounding the tower exerts a substantial influence on pollutant concentration through two key mechanisms. First, pressure gradients shape the velocity field, driving the formation of wake vortices that capture pollutants and elevate local concentrations. Ginger & Letchford [59], He et al. [60]and Tominaga & Stathopoulos [61] explained that these vortices emerge from flow separation induced by the tower's bluff geometry, where high-pressure areas on the windward side contrast sharply with low-pressure regions in the leeward wake Figure 11e, fostering recirculation zones that retain pollutants. This pressure disparity arises as wind collides with the tower's front face, pushing the flow upward toward the roof. Upon reaching the roof's leading edge, the flow separates and accelerates around the corner. This acceleration (Fig. 9b) causes a localized pressure drop, consistent with the Bernoulli effect, which contributes to vortex formation. Second, pressure gradients regulate the vertical movement of pollutants and influence vertical mixing. Low-pressure zones in the wake produce a pronounced suction effect (Figure 11g) which induces significant upward flow, lifting pollutants such as fine particulate matter (e.g., PM2.5) into higher atmospheric layers, thereby altering their vertical distribution. This suction arises from the rapid flow acceleration around the tower's edges. These low-pressure regions draw air and pollutants from surrounding higher-pressure areas, creating vertical currents that transport pollutants upward, potentially reducing ground-level concentrations while

increasing exposure at elevated heights. Conversely, high-pressure zones on the windward side suppress vertical mixing, causing pollutants to remain closer to the ground and increasing local concentrations near the surface [62].

This dual influence of pressure gradients is critical for understanding pollutant dispersion patterns, as it governs both horizontal trapping Figure 11 c and vertical redistribution across different heights. The suction effect in the wake is particularly significant in urban environments like in this study, where tall structures like the tower create complex flow patterns that can exacerbate or mitigate pollution hotspots depending on atmospheric conditions. This vertical transport mechanism is supported by Gousseau et al. [63], who used large-eddy simulation to show that low-pressure wake regions behind a cubic building induce upward velocity components, enhancing pollutant dispersion to higher altitudes. Similarly, Gousseau [64] demonstrated through CFD simulations that pressure-driven flows in the wake of building groups in Montreal promote vertical pollutant transport, influencing concentration distributions at various heights.

## 5. Conclusion

In suumary, the detailed interactions between turbulent flow and pollutant concentration around the Keangnam Hanoi Landmark Tower have been thoroughly studied for the first time by using LBE combined with block-structured topology-confined mesh refinement, with a focus on urban aerodynamic challenges. The computational setup employed a block-structured, topology-confined mesh refinement strategy to capture flow dynamics around the towers. The model, built using SALOME from AutoCAD drawings, featured smooth, rigid towers.

- The computational domain measured $22D$ (streamwise), $12D$ (spanwise), and $10D$ (vertical) to ensure sufficient spatial resolution, where $D$ is a normalized length scale ($D = 93\,m$). Boundary conditions included a uniform inlet velocity of $0.9677\ m/s$, free-slip conditions on lateral and upper boundaries, no-slip conditions on ground and tower surfaces via half-way bounce-back and Immersed Boundary Methods, and an open outflow condition ($\partial \mathrm{u}/\partial \mathrm{x} = 0$).

- A three-level mesh refinement with cell sizes Δ, 2Δ, and 4Δ focused on boundary layers and shear layers, using uniform cell distribution within cubic blocks to determine the total grid count based on boundary layer thickness ($\delta_B$).

- The simulation's fidelity was verified by assessing the spatial grid size ($\Delta x$) and time step ($\Delta t$) against Kolmogorov scales, which define the smallest turbulent dissipation scales. These scales, derived from kinematic viscosity ($\nu$) and energy dissipation rate ($\varepsilon$), represent the threshold where viscous dissipation balances energy transfer across eddy scales. Validation criteria required $\Delta x/\eta < 5$ and $\Delta t/\tau < 1$ in critical regions.

- The domain was discretized into 5 planes along each axis, totalling 15 sections, where these conditions were evaluated. This analysis verified by showing that all the criteria are respected for each plan that the selected grid size and time step effectively resolved turbulent fluctuations, ensuring precise flow dynamics capture.

- The pollutant distribution closely follows the simulated velocity streamlines due to the high Peclet numbers (Pe $\gg$ 1) throughout the domain. The advection–diffusion equation shows that advection by the mean wind predominates over molecular diffusion. Paraview visualizations of instantaneous streamlines reveal large-scale recirculation zones downstream of the tower. These zones act as effective pollutant traps: the bluff geometry induces flow separation, generating regions where reduced velocities hinder downstream transport. This stagnation effect limits pollutant removal, allowing concentrations

to accumulate in localized areas. Furthermore, limited mixing within these regions sustains high pollutant levels in the wake over extended periods.

- Pressure gradients around the tower significantly influence pollutant distribution by shaping wake vortices and limiting vertical mixing. High-to-low pressure transitions induce recirculation zones that trap pollutants horizontally, while low-pressure regions in the wake generate upward flows, redistributing pollutants vertically. These mechanisms reinforce both accumulation near the structure and dispersion across different heights.

This study offers a refined numerical analysis of pollutant dispersion around the Keangnam Hanoi Landmark Tower using the Lattice Boltzmann Method combined with block-structured, topology-confined mesh refinement. While similar approaches have been explored in urban flow research, the present work stands out by applying this methodology to a highly specific and realistic high-rise building complex with triangular and curved geometries an urban configuration that remains rarely addressed. The simulation's accuracy is confirmed through validation based on Kolmogorov scales, ensuring proper resolution of turbulent structures. These contributions provide new understanding of pollutant dynamics in dense urban environments and offer valuable insights for future studies in urban aerodynamics and air quality management.

To finish this work, it would be valuable to extend the study by modifying the input data, specifically by varying wind speed, wind direction, and the location of the pollution source through additional simulations. These variations would allow for testing the robustness of the current findings and provide a deeper understanding of pollutant dispersion mechanisms in complex urban environments. Particular attention should also be given to the evolution and dissipation of vortex structures in the wake of the building, as they play a critical role in pollutant transport and retention.

Furthermore, this numerical investigation paves the way for complementary experimental studies. It is recommended to implement pollution measurement devices at different heights on high-rise buildings such as the Keangnam Tower. This would help assess more accurately the impact of air pollution on residents and pedestrians, validate simulation results, and better understand the health implications associated with vertical air quality distribution in urban areas.

## References

[1] World Health Organisation, WHO Global Air Quality Guidelines: Particulate Matter (PM2.5 and PM10), Ozone, Nitrogen Dioxide, Sulfur Dioxide and Carbon Monoxide, World Health Organisation, Geneva, 2021.

[2] K. He, Q. Zhang, D. Ming, Y. Wu, C. Witherspoon, V. Foltescu, Y. Han, J. Cheng, Y. Qu, A Review of 20 Years' Air Pollution Control in Beijing, United Nations Environment Programme, Nairobi, 2019.

[3] European Environment Agency, Air Quality in Europe 2021, European Environment Agency, Copenhagen, 2021.

[4] Z. Li, T. Ming, S. Liu, C. Peng, R. D. Richter, W. Li, H. Zhang, C. Y. Wen, Review on Pollutant Dispersion in Urban Areas-Part A: Effects of Mechanical Factors and Urban Morphology, Building and Environment, Vol. 190, 2021, pp. 107534, https://doi.org/10.1016/j.buildenv.2020.107534.

[5] X. Zhang, X. Chen, X. Zhang, The Impact of Exposure to Air Pollution on Cognitive Performance, Proceedings of the National Academy of Sciences, Vol. 115, No. 37, 2018, pp. 9193-9197, https://doi.org/10.1073/pnas.1809474115.

[6] Organisation for Economic Co-operation and Development (OECD), The Economic Consequences of Outdoor Air Pollution, OECD Publishing, Paris, 2016.

[7] R. Yu, Correlation Analysis of Urban Building Form and PM2.5 Pollution Based on Satellite and Ground Observations, Frontiers in Environmental Science, Vol. 10, 2023, pp. 1111223, https://doi.org/10.3389/fenvs.2022.1111223.

[8] C. Lee, How Do Built Environments Measured at Two Scales Influence PM2.5 Concentrations, Transportation Research Part D: Transport and Environment, Vol. 99, 2021, pp. 103014, https://doi.org/10.1016/j.trd.2021.103014.

[9] J. Hang, Y. Li, M. Sandberg, R. Buccolieri, S. D. Sabatino, The Influence of Building Height Variability on Pollutant Dispersion and Pedestrian Ventilation in Idealized High-Rise Urban Areas, Building and Environment, Vol. 56, 2012, pp. 346-360, https://doi.org/10.1016/j.buildenv.2012.03.024.

[10] B. Blocken, Computational Fluid Dynamics for Urban Physics: Importance, Scales, Possibilities, Limitations and Ten Tips and Tricks Towards Accurate and Reliable Simulations, Building and Environment, Vol. 91, 2015, pp. 219-245, https://doi.org/10.1016/j.buildenv.2015.02.015.

[11] Y. Tominaga, T. Stathopoulos, CFD Simulation of Near-Field Pollutant Dispersion in the Urban Environment: A Review of Current Modeling Techniques, Atmospheric Environment, Vol. 79, 2013, pp. 716-730, https://doi.org/10.1016/j.atmosenv.2013.07.028.

[12] Y. Zhang, K. C. S. Kwok, X. P. Liu, J. L. Niu, Characteristics of Air Pollutant Dispersion Around a High-Rise Building, Environmental Pollution, Vol. 204, 2015, pp. 280-288, https://doi.org/10.1016/j.envpol.2015.05.006.

[13] M. Lateb, R. N. Meroney, M. Yataghene, H. Fellouah, F. Saleh, M. C. Boufadel, On the Use of Numerical Modelling for Near-Field Pollutant Dispersion in Urban Environments- A Review, Environmental Pollution, Vol. 208, 2016, pp. 271-283, https://doi.org/10.1016/j.envpol.2015.07.031.

[14] S. J. Mei, Z. Luo, F. Y. Zhao, H. Q. Wang, Street Canyon Ventilation and Airborne Pollutant Dispersion: 2-D Versus 3-D CFD Simulations, Sustainable Cities and Society, Vol. 50, 2019, pp. 101700, https://doi.org/10.1016/j.scs.2019.101700.

[15] E. Aristodemou, L. M. Boganegra, L. Mottet, D. Pavlidis, A. Constantinou, C. Pain, A. Robins, H. ApSimon, How Tall Buildings Affect Turbulent Air Flows and Dispersion of Pollution Within a Neighbourhood, Environmental Pollution, Vol. 233, 2018, pp. 782-796, https://doi.org/10.1016/j.envpol.2017.10.053.

[16] S. H. Peng, L. Davidson, Comparison of Subgrid-Scale Models in LES for Turbulent Convection Flow with Heat Transfer, Second International Symposium on Turbulent Heat Transfer, Begell House, New York, 1998, pp. 5-24.

[17] S. Succi, Lattice Boltzmann 2038, Europhysics Letters, Vol. 109, No. 5, 2015, pp. 50001, https://doi.org/10.1209/0295-5075/109/50001.

[18] F. J. Higuera, J. Jiménez, Boltzmann Approach to Lattice Gas Simulations, Europhysics Letters, Vol. 9, No. 7, 1989, pp. 663-668, https://doi.org/10.1209/0295-5075/9/7/009.

[19] F. J. Higuera, J. Jiménez, Boltzmann Approach to Lattice Gas Simulations, Europhysics Letters, Vol. 9, No. 7, 1989, pp. 663-668, https://doi.org/10.1209/0295-5075/9/7/009.

[20] F. J. Higuera, S. Succi, Simulating the Flow Around a Circular Cylinder with a Lattice Boltzmann Equation, Europhysics Letters, Vol. 8, No. 6, 1989, pp. 517-521, https://doi.org/10.1209/0295-5075/8/6/005.

[21] A. J. C. Ladd, R. Verberg, Lattice-Boltzmann Simulations of Particle-Fluid Suspensions, Journal of Statistical Physics, Vol. 104, No. 5, 2001, pp. 1191-1251, https://doi.org/10.1023/A:1010414013942.

[22] S. Chen, G. D. Doolen, Lattice Boltzmann Method for Fluid Flows, Annual Review of Fluid Mechanics, Vol. 30, No. 1, 1998, pp. 329-364, https://doi.org/10.1146/annurev.fluid.30.1.329.

[23] D. V. Duong, L. Van Nguyen, D. Van Nguyen, T. C. Dinh, L. R. Zuhal, L. I. Ngo, Direct Numerical Simulation of 45° Oblique Flow Past Surface-Mounted Square Cylinder, Journal of Fluid Mechanics, Vol. 992, 2024, pp. A12, https://doi.org/10.1017/jfm.2024.394.

[24] K. Suga, Y. Kuwata, K. Takashima, R. Chikasue, A D3Q27 Multiple-Relaxation-Time Lattice Boltzmann Method for Turbulent Flows, Computers & Mathematics with Applications, Vol. 69, No. 6, 2015, pp. 518-529, https://doi.org/10.1016/j.camwa.2015.01.010.

[25] K. Huang, Statistical Mechanics, John Wiley & Sons, Hoboken, NJ, 2008.

[26] L. Wang, Enhanced Multi-Relaxation-Time Lattice Boltzmann Model by Entropic Stabilizers, Physical Review E, Vol. 102, No. 2, 2020, p. 023307, https://doi.org/10.1103/PhysRevE.102.023307.

[27] P. Lallemand, L. S. Luo, Theory of the Lattice Boltzmann Method: Dispersion, Dissipation, Isotropy, Galilean Invariance, and Stability, Physical Review E, Vol. 61, No. 6, 2000, pp. 6546-6562, https://doi.org/10.1103/PhysRevE.61.6546.

[28] F. Dubois, P. Lallemand, Quartic Parameters for Acoustic Applications of Lattice Boltzmann Scheme, Computers & Mathematics with Applications, Vol. 61, No. 12, 2011, pp. 3404-3416, https://doi.org/10.1016/j.camwa.2011.01.011.

[29] T. Möller, B. Trumbore, Fast, Minimum Storage Ray/Triangle Intersection, ACM SIGGRAPH 2005 Courses, 2005, pp. 7, https://doi.org/10.1145/1198555.1198746.

[30] M. Bouzidi, M. Firdaouss, P. Lallemand, Momentum Transfer of a Boltzmann-Lattice Fluid with Boundaries, Physics of Fluids, Vol. 13, No. 11, 2001, pp. 3452-3459, https://doi.org/10.1063/1.1399290.

[31] Y. Chen, Q. Cai, Z. Xia, M. Wang, S. Chen, Momentum-Exchange Method in Lattice Boltzmann Simulations of Particle-Fluid Interactions, Physical Review E—Statistical, Nonlinear, and Soft Matter Physics, Vol. 88, No. 1, 2013, pp. 013303, https://doi.org/10.1103/PhysRevE.88.013303.

[32] V. D. Duong, V. D. Nguyen, V. T. Nguyen, I. L. Ngo, Low-Reynolds-Number Wake of Three Tandem Elliptic Cylinders, Physics of Fluids, Vol. 34, No. 4, 2022, pp. 043605, https://doi.org/10.1063/5.0086685.

[33] T. Kamatsuchi, Turbulent Flow Simulation Around Complex Geometries with Cartesian Grid Method, 45th AIAA Aerospace Sciences Meeting and Exhibit, 2007, pp. 1459, https://doi.org/10.2514/6.2007-1459.

[34] T. Ishida, S. Takahashi, K. Nakahashi, Efficient and Robust Cartesian Mesh Generation for Building-Cube Method, Journal of Computational Science and Technology, Vol. 2, No. 4, 2008, pp. 435-446, https://doi.org/10.1299/jcst.2.435.

[35] M. Bader, Space-Filling Curves: An Introduction with Applications in Scientific Computing, Springer Science & Business Media, Berlin, Heidelberg, 2012, https://doi.org/10.1007/978-3-642-31046-1.

[36] Y. Tamura, T. Ohkuma, H. Kawai, Y. Uematsu, K. Kondo, Revision of AIJ Recommendations for Wind Loads on Buildings, Structures 2004: Building on the Past, Securing the Future, 2004, pp. 1-10, https://doi.org/10.1061/40700(2004)24.

[37] Y. Cao, T. Tamura, D. Zhou, Y. Bao, Z. Han, Topological Description of Near-Wall Flows Around a Surface-Mounted Square Cylinder at High Reynolds Numbers, Journal of Fluid Mechanics, Vol. 933, 2022, pp. A39, https://doi.org/10.1017/jfm.2021.1094.

[38] C. Shu, L. L. Wang, M. Mortezazadeh, Dimensional Analysis of Reynolds Independence and Regional Critical Reynolds Numbers for Urban Aerodynamics, Journal of Wind Engineering and Industrial Aerodynamics, Vol. 203, 2020, pp. 104232, https://doi.org/10.1016/j.jweia.2020.104232.

[39] B. Blocken, T. Stathopoulos, J. Carmeliet, CFD Simulation of the Atmospheric Boundary Layer: Wall Function Problems, Atmospheric Environment, Vol. 41, No. 2, 2007, pp. 238-252, https://doi.org/10.1016/j.atmosenv.2006.08.019.

[40] J. Franke, A. Hellsten, K. H. Schlunzen, B. Carissimo, The COST 732 Best Practice Guideline for CFD Simulation of Flows in the Urban Environment: A Summary, International Journal of Environment and Pollution, Vol. 44, No. 1-4, 2011, pp. 419-427, https://doi.org/10.1504/IJEP.2011.038443.

[41] G. Falcucci, M. Aureli, S. Ubertini, M. Porfiri, Transverse Harmonic Oscillations of Laminae in Viscous Fluids: A Lattice Boltzmann Study, Philosophical Transactions of the Royal Society A: Mathematical, Physical and Engineering Sciences, Vol. 369, No. 1945, 2011, pp. 2456-2466, https://doi.org/10.1098/rsta.2011.0069.

[42] S. Succi, The Lattice Boltzmann Equation: for Fluid Dynamics and Beyond, Oxford University Press, Oxford, 2001.

[43] A. J. C. Ladd, Numerical Simulations of Particulate Suspensions via a Discretized Boltzmann Equation. Part 1. Theoretical Foundation, Journal of Fluid Mechanics, Vol. 271, 1994, pp. 285-309, https://doi.org/10.1017/S002211209400177X.

[44] F. M. White, J. Majdalani, Viscous Fluid Flow, McGraw-Hill, New York, 2006.

[45] Y. Li, J. Zhang, G. Dong, N. S. Abdullah, Small-Scale Reconstruction in Three-Dimensional Kolmogorov Flows Using Four-Dimensional Variational Data Assimilation, Journal of Fluid Mechanics, Vol. 885, 2020, pp. A9, https://doi.org/10.1017/jfm.2019.980.

[46] P. Moin, K. Mahesh, Direct Numerical Simulation: A Tool in Turbulence Research, Annual Review of Fluid Mechanics, Vol. 30, No. 1, 1998, pp. 539-578, https://doi.org/10.1146/annurev.fluid.30.1.539.

[47] A. Yakhot, H. Liu, N. Nikitin, Turbulent Flow Around a Wall-Mounted Cube: A Direct Numerical Simulation, International Journal of Heat and Fluid Flow, Vol. 27, No. 6, 2006, pp. 994-1009, https://doi.org/10.1016/j.ijheatfluidflow.2006.03.003.

[48] S. Malik, S. T. Ejaz, A. Akgül, M. K. Hassani, Exploring the Advection-Diffusion Equation Through the Subdivision Collocation Method: A Numerical Study, Scientific Reports, Vol. 14, No. 1, 2024, pp. 1712, https://doi.org/10.1038/s41598-024-52199-6.

[49] R. Szymkiewicz, D. Gąsiorowski, Adaptive Method for the Solution of 1D and 2D Advection--Diffusion Equations Used in Environmental Engineering, Journal of Hydroinformatics, Vol. 23, No. 6, 2021, pp. 1290-1311, https://doi.org/10.2166/hydro.2021.144.

[50] E. Batchvarova, S. -E. Gryning, Progress in Urban Dispersion Studies, Theoretical and Applied Climatology, Vol. 84, No. 1, 2006, pp. 57-67, https://doi.org/10.1007/s00704-005-0130-y.

[51] A. Venkatram, J. Upadhyay, J. Yuan, J. Heumann, J. Klewicki, The Development and Evaluation of a Dispersion Model for Urban Areas, Fourth AMS Symposium on the Urban Environment, Norfolk, VA, 2002.

[52] R. E. Britter, S. R. Hanna, Flow and Dispersion in Urban Areas, Annual Review of Fluid Mechanics, Vol. 35, No. 1, 2003, pp. 469-496, https://doi.org/10.1146/annurev.fluid.35.101101.161147.

[53] H. D. Lim, D. Hertwig, T. Grylls, H. Gough, M. van Reeuwijk, S. Grimmond, C. Vanderwel, Pollutant Dispersion by Tall Buildings: Laboratory Experiments and Large-Eddy Simulation, Experiments in Fluids, Vol. 63, No. 6, 2022, pp. 92, https://doi.org/10.1007/s00348-022-03445-5.

[54] D. Hertwig, H. L. Gough, S. Grimmond, J. F. Barlow, C. W. Kent, W. E. Lin, A. G. Robins, P. Hayden, Wake Characteristics of Tall Buildings in a Realistic Urban Canopy, Boundary-Layer Meteorology, Vol. 172, No. 2, 2019, pp. 239-270, https://doi.org/10.1007/s10546-019-00451-8.

[55] T. Rich, C. Vanderwel, Pollutant Dispersion Around a Single Tall Building, Boundary-Layer Meteorology, Vol. 190, No. 8, 2024, pp. 34, https://doi.org/10.1007/s10546-024-00912-7.

[56] Y. Fu, Y. Wang, P. Yang, Y. Li, H. Liu, T. K. T. Tse, C. Y. Li, K. He, B. Zhang, Gap Flow Dynamics and Air Pollutant Dispersion Mechanism Behind Building Clusters, Physics of Fluids, Vol. 37, No. 3, 2025, https://doi.org/10.1063/5.0210217.

[57] C. H. Moeng, R. Rotunno, I. R. Paluch, Vertical-Velocity Skewness in the Marine Stratus-Topped Boundary Layer, NASA, Langley Research Center, FIRE Science Results 1989, 1990.

[58] S. Kida, H. Miura, Identification and Analysis of Vortical Structures, European Journal of Mechanics-B/Fluids, Vol. 17, No. 4, 1998, pp. 471-488, https://doi.org/10.1016/S0997-7546(98)80017-8.

[59] J. D. Ginger, C. W. Letchford, Characteristics of Large Pressures in Regions of Flow Separation, Journal of Wind Engineering and Industrial Aerodynamics, Vol. 49, No. 1-3, 1993, pp. 301-310, https://doi.org/10.1016/0167-6105(93)90027-F.

[60] H. He, D. Ruan, K. C. Mehta, X. Gilliam, F. Wu, Nonparametric Independent Component Analysis for Detecting Pressure Fluctuation Induced by Roof Corner Vortex, Journal of Wind Engineering and Industrial Aerodynamics, Vol. 95, No. 6, 2007, pp. 429-443, https://doi.org/10.1016/j.jweia.2006.09.002.

[61] Y. Tominaga, T. Stathopoulos, Numerical Simulation of Dispersion Around an Isolated Cubic Building: Model Evaluation of RANS and LES, Building and Environment, Vol. 45, No. 10, 2010, pp. 2231-2239, https://doi.org/10.1016/j.buildenv.2010.04.004.

[62] B. Blocken, T. Stathopoulos, J. P. A. J. V. Beeck, Pedestrian-Level Wind Conditions Around Buildings: Review of Wind-Tunnel and CFD Techniques and Their Accuracy for Wind Comfort Assessment, Building and Environment, Vol. 100, 2016, pp. 50-81, https://doi.org/10.1016/j.buildenv.2016.02.004.

[63] P. Gousseau, B. Blocken, G. J. F. Van Heijst, Large-Eddy Simulation of Pollutant Dispersion Around a Cubical Building: Analysis of the Turbulent Mass Transport Mechanism by Unsteady Concentration and Velocity Statistics, Environmental Pollution, Vol. 167, 2012, pp. 47-57, https://doi.org/10.1016/j.envpol.2012.03.056.

[64] P. Gousseau, B. J. E. Blocken, T. Stathopoulos, G. J. F. van Heijst, Large-Eddy Simulation of Pollutant Dispersion in Downtown Montreal: Evaluation of the Convective and Turbulent Mass Fluxes, International Congress on Environmental Modelling and Software: Managing Resources of a Limited Planet, Leipzig, Germany, 2012, pp. 1-8.